Composites Part B 268 (2024) 111056

Contents lists available at ScienceDirect

Composites Part B

journal homepage: www.elsevier.com/locate/compositesb

Significant improvement of the room and cryogenic mechanical properties of an AlN particle reinforced Al matrix composite by alloying element magnesium

Xinda Sun [a,1], Yong Fan [a,1], Jinfeng Nie [a,*], Yuyao Chen [a], Kewei Xie [b], Sida Liu [c,**], Yonghao Zhao [a], Xiangfa Liu [b]

[a] Nano and Heterogeneous Materials Center, School of Materials Science and Engineering, Nanjing University of Science and Technology, Nanjing, 210094, China
[b] Key Laboratory for Liquid–Solid Structural Evolution and Processing of Materials, Ministry of Education, Shandong University, Jinan, 250061, China
[c] Laboratory for Multiscale Mechanics and Medical Science, SV LAB, School of Aerospace, Xi'an Jiaotong University, Xi'an, 710049, China

ARTICLE INFO

Handling Editor: Dr Hao Wang

Keywords:
Aluminum matrix composites
Liquid-solid reaction
Mg element
Cryogenic properties

ABSTRACT

Nowadays, the mechanical properties of aluminum alloys have been studied extensively, but the study of aluminum matrix composites (AMCs) at extreme temperatures, particularly at cryogenic temperatures, is rare. In this work, an AlN_p reinforced AMCs with excellent room and cryogenic temperature mechanical properties was manufactured by adding magnesium, and the corresponding microstructure evolution and strengthening mechanisms were systematically investigated. There are two kinds of particles in AlN_p/Al, the small AlN_p and the large AlB_{2p}. With the Mg content increased, the AlN_p became more dispersed and the AlB_{2p} transformed into $AlMgB_{4p}$. In addition, Mg atoms also dissolved in the matrix, which played a positive role in improving the mechanical properties. The ultimate tensile strength of the composites at RT was increased to 317 MPa, 419 MPa, and 485 MPa from 251 MPa after adding 1, 3, and 5 wt% Mg respectively. The cryogenic strength was further increased to 519 MPa, 592 MPa, and 611 MPa from 469 MPa, while keeping a decent ductility of about 5.6%, which was due to the more uniform microstructure avoiding crack generation.

1. Introduction

For a long time, aluminum and its alloys have been widely used in aerospace, automotive, etc. due to their high specific intensity, corrosion resistance [1], etc. The wide service temperature range not only requires a good property at room temperature (RT) but also places high demands on the maintenance of properties at extreme temperatures. Up to now, there have been many relatively comprehensive studies to explore the application of Al alloys at extreme temperatures. Sun et al. [2] have produced an excellent heat-resistant Al alloy and investigated the strengthening mechanisms in detail. The simultaneous increase in strength and ductility of Al alloys at cryogenic temperatures has also been widely reported [3]. However, the high strength of Al alloys is mainly achieved by adding alloying elements and subsequent heat treatment. The complex interaction between alloying elements makes a high demand on processing design. Compared to Al alloys, aluminum matrix composites (AMCs) typically have a higher specific modulus and structural stability [4], and are increasingly being used in structural and functional materials [5]. Current researches about AMCs mainly focus on microstructural adjustment, RT and high temperature properties, but rarely on the mechanical properties at cryogenic environments [6,7].

Actually, the properties of composites are determined by numerous factors, and selecting various combinations of matrix and particles is a widely used method to enhance the comprehensive mechanical properties [8,9]. In addition, the particle size and distribution also have a significant effect on the properties, which are largely influenced by the manufacturing process [10]. Yang et al. [11] have demonstrated that, during the tensile deformation at RT, the presence of large particles and particle aggregation zones may cause cracking or debonding with the matrix, potentially becoming a source of cracks. It will lead to premature failure of the AMCs, which is not the case for most of Al alloys that experience a simultaneous increase in strength and ductility when

* Corresponding author.
** Corresponding author.
E-mail addresses: niejinfeng@njust.edu.cn (J. Nie), sidaliu@xjtu.edu.cn (S. Liu).
[1] These authors contributed equally to this work.

https://doi.org/10.1016/j.compositesb.2023.111056
Received 5 September 2023; Received in revised form 10 October 2023; Accepted 15 October 2023
Available online 20 October 2023

subjected to cryogenic temperatures. Compared to particles generated ex-situ, in-situ particles generated directly within the matrix possess a smaller diameter, a more uniform distribution, and typically exhibit a superior binding interface with the matrix [12]. These advantages are beneficial in increasing the RT properties of the composites and maintaining them in extreme temperature environments. Therefore, in-situ particle reinforced AMCs are more likely to retain a sufficient ductility at cryogenic temperatures. Many types of in-situ reinforcing particles have been synthesized in AMCs, such as TiB_2, Al_3Ti, TiC, ZrB_2 [13] and AlN [14]. Among them, AlN particles (AlN_p) have a relatively smooth shape with no obvious angles, which can avoid cracking caused by stress concentration. In addition, AlN_p has several well-matched lattice orientations with Al matrix, allowing for a tight interfacial bonding [15,16]. Therefore, it is a viable project to choose AlN_p as the reinforcing particle, in order to obtain a good cryogenic properties.

Furthermore, the primary strengthening mechanisms of the reinforcing particles in AMCs are Orowan strengthening and load transfer strengthening. The strengthening effect is limited at low particle contents, but the dislocation storage capacity of matrix will be severely reduced at high particle contents, resulting in a significant loss of ductility. Significant strengthening has been achieved in Al alloys by combining different alloying elements, while the reaction between multiple alloying elements and the particles will be complex [17,18], especially during the in-situ reaction process. Therefore, selecting a few kinds or just one kind of alloying element combined with appropriate particle content to strengthen AMCs is a reasonable solution. Magnesium atoms have a high solubility and good solid solution strengthening effect in the Al matrix, and previous studies have also shown that Al–Mg alloys exhibit an excellent cryogenic strength and ductility [19]. However, when the Mg content is above 5 wt%, the brittle β-Al_3Mg_2 phase will form in the Al–Mg alloy, leading to the deterioration of the mechanical properties [20]. To avoid the enrichment of excessive alloying elements surrounding the particles and the generation of harmful phases, the Mg content should be limited.

This work aims to provide a viable strategy for optimizing the microstructure and the mechanical properties of AMCs. In-situ AlN_p reinforced Al-xMg (x = 0, 1, 3, 5%) matrix composites were produced by hot sintering and hot extrusion. The evolution of microstructure and the mechanical properties were investigated. The reasons for the evolution of the morphology and distribution of the reinforcing particles were discussed. The combined strengthening mechanism of the reinforcing particles and alloying elements was analyzed.

2. Materials and methods

2.1. Manufacturing process of AlN_p/Al-xMg composites

The AlN_p reinforced aluminum matrix composite of this work was manufactured by powder sintering and subsequent hot extrusion, as shown in Fig. 1. The raw materials are commercial Al powders (99.7 wt % purity, particle diameter ~15 μm), Al–50Mg alloy powders (particle diameter ~50 μm) and boride nitrogen powders (98.5 wt% purity, particle diameter ~0.5–1 μm) supplied by Shandong Al&Mg Melt Technology Co. Ltd. (Jinan, China). The morphologies of raw powders are shown in Fig. 2a and b, and the composites with different percentages of magnesium were achieved by adjusting the addition of Al–50Mg powders. The raw material powders with different proportions were combined by ball-milling for 4 h in an argon atmosphere (the morphologies of ball-milled powders are shown in Fig. 2c and d), and then the powder mixture was cold-pressed in a cold isostatic press machine. Subsequently, the 8.2 wt% AlN_p reinforced Al-xMg (x = 0, 1, 3, 5 wt%) composites were fabricated by liquid-solid reaction at 800 °C for 1 h, under an argon atmosphere without extra pressure. Finally, the composites were extruded at 500 °C with a 9:1 extrusion ratio to obtain the composite rods with a diameter about 30 mm.

2.2. Characterization and mechanical property testing

The microstructures of AlN_p/Al-xMg specimens were characterized by a field emission scanning electron microscope (FESEM, Quanta 250F, FEI, Hillsboro, OR, USA, work voltage 15 kV, work distant 10 mm) equipped with an energy dispersive spectroscopy (EDS, Oxford Instruments, Oxford, UK), electron back-scattered diffraction (EBSD, Zeiss, Jena, Thuringia, DE, work voltage 15 kV, sample angle 70°) and a transmission electron microscope (TEM, FEI, Hillsboro, USA, work voltage 200 kV). The samples for microstructure observation were etched with 0.5 vol% hydrofluoric acid after mechanical polishing. The EBSD data was analyzed using the Channel 5 software.

The tensile properties were determined using Walter + bai LFM 20 kN universal testing machine for uniaxial tensile testing at RT and liquid nitrogen temperature (LNT) with the strain rate of 10^{-3} s^{-1}. The gauge size of the tensile test specimen was 10 mm in length and 2.5 mm in width, and the loading direction was parallel to the extrusion direction (ED) of the rod.

2.3. Calculation method

The first-principles calculations were performed using Vienna ab initio simulation package (VASP) code with the project-augmented wave method and the Perdew-Burke-Ernzerhof version of the exchange correlation functional [21,22]. During VASP calculations, a Monkhorst-Pack k-point mesh of 9 × 9 × 9 was applied and the cutoff energy of the plane wave basis was set as 500 eV for AlB_2 and MgB_2. For Al_3MgB_8, $AlMgB_4$, and $AlMg_3B_8$ the Monkhorst-Pack k-point mesh was set 9 × 9 × 4.

For the electronic relaxation processes and the ionic relaxation loop, the convergence criterion is set to 10^{-4} eV and 0.02 GPa, respectively. Besides, The P6/mmm structure TMB_2, α-metal, and α-B were used to calculate the formation enthalpies. The enthalpy of formation (ΔH_{form}) can calculated as follows [23]:

$$\Delta H_{form} = \frac{1}{N}\left[E_{Total} - \sum_{i=1}^{N} E_i^{bulk}\right] \quad (1)$$

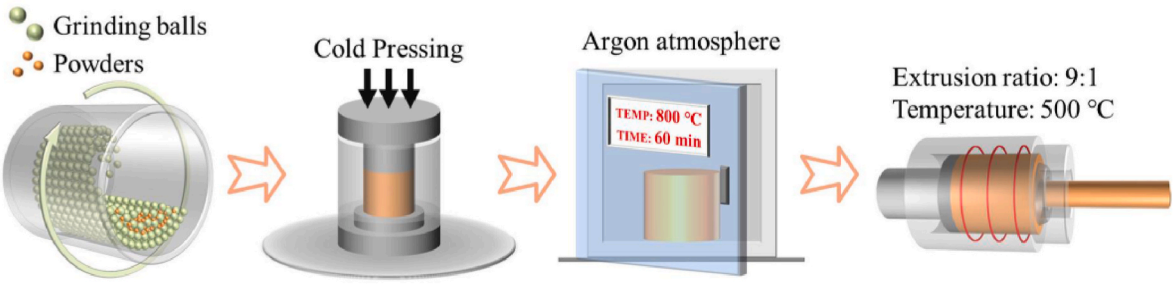

Fig. 1. Schematic diagram of the preparation process of AlN_p/Al-xMg composites.

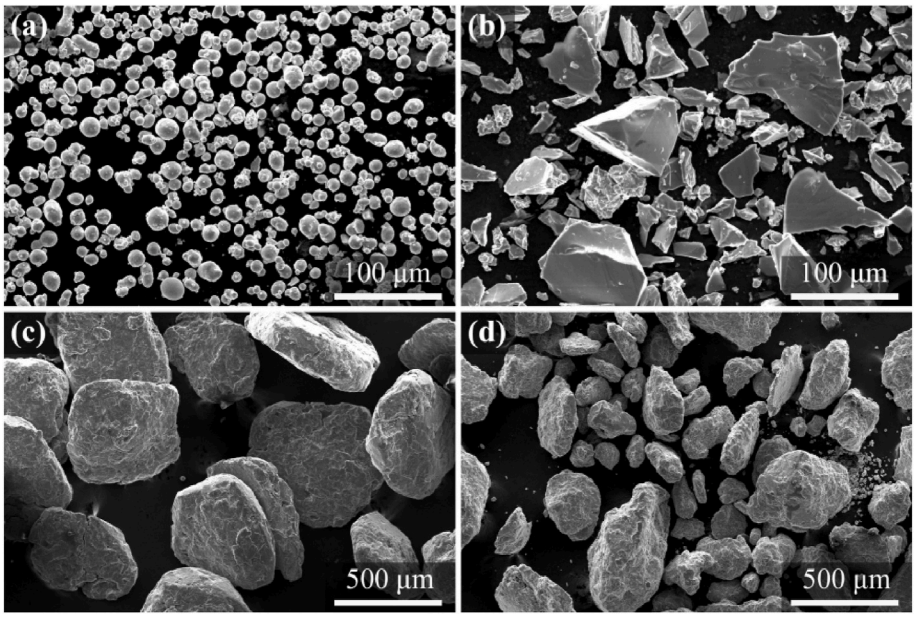

Fig. 2. The morphologies of (a) Al powders and (b) Al–50Mg alloy powders; ball-milled (c) AlN_p/Al powders and (d) AlN_p/Al–5Mg powders.

Where N is the amount of atoms in the cell; E_{Total} and $Ebulk\ i$ represent the total energy of the bulk compound and energy per atom in solid states, respectively.

3. Results

3.1. Morphology and distribution of the reinforcement particles in AlN_p/Al-xMg

The morphology of the sample before extrusion is shown in Fig. S1. Because the extrusion temperature (500 °C) is lower than the reaction temperature (580 °C) and the holding time before extrusion is short, there is no change in the particle type before and after the extrusion. Fig. 3 shows the microstructure of the extruded AlN_p/Al-xMg samples. Two kinds of reinforcing particles could be observed in AlN_p/Al (Fig. 3a), the larger particle was AlB_{2p} (black in color) and the smaller was AlN_p (pale grey in color). Corresponding EDS elemental analyses are shown in Fig. 4a. The AlN_p was distributed along the extrusion direction in the winding band zone, and many particle-free zones could be observed. After adding 1% Mg, the larger particle diameter was significantly reduced and the boundary of the AlN_p-rich zone and AlN_p-free zone became straighter. Further increase the Mg content, the particle-

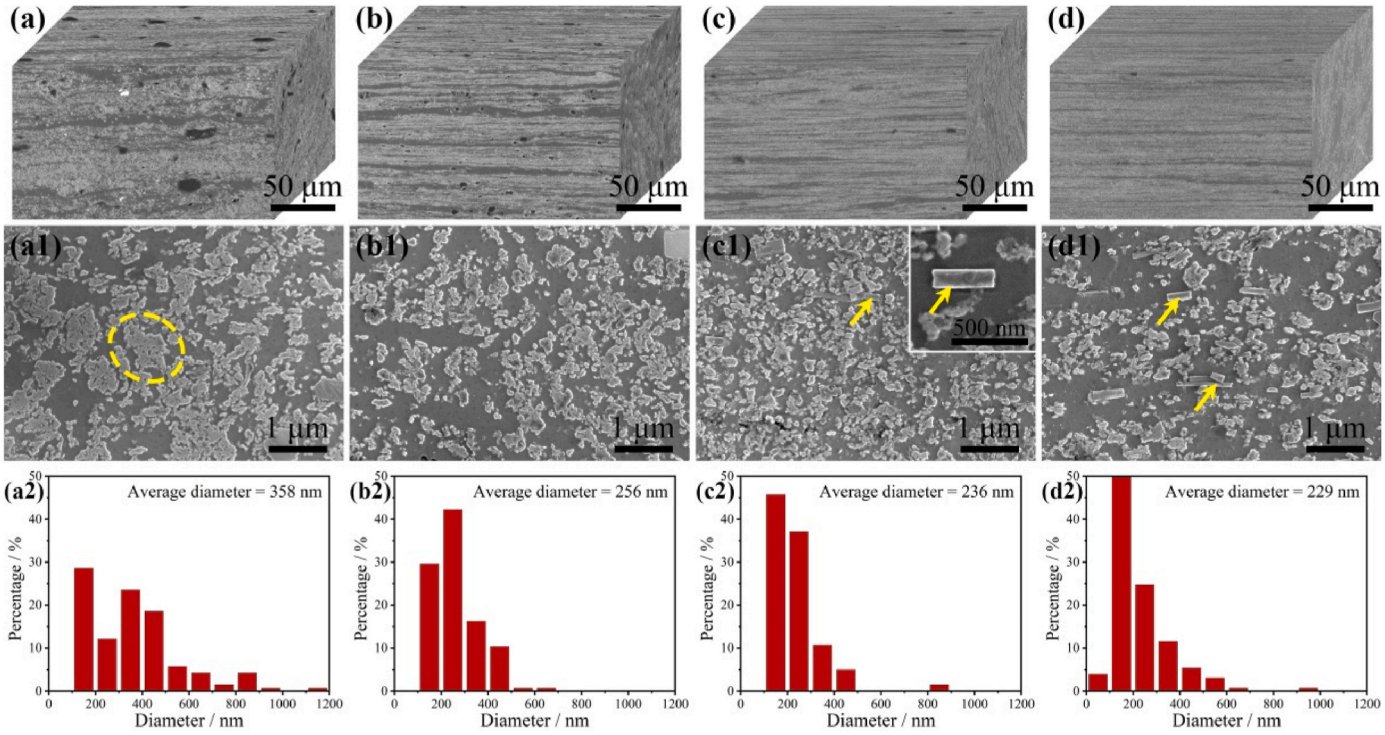

Fig. 3. The SEM morphologies and agglomerated AlN_p diameter statistics of (a-a2) AlN_p/Al; (b-b2) AlN_p/Al–1Mg; (c-c2) AlN_p/Al–3Mg and (d-d2) AlN_p/Al–5Mg.

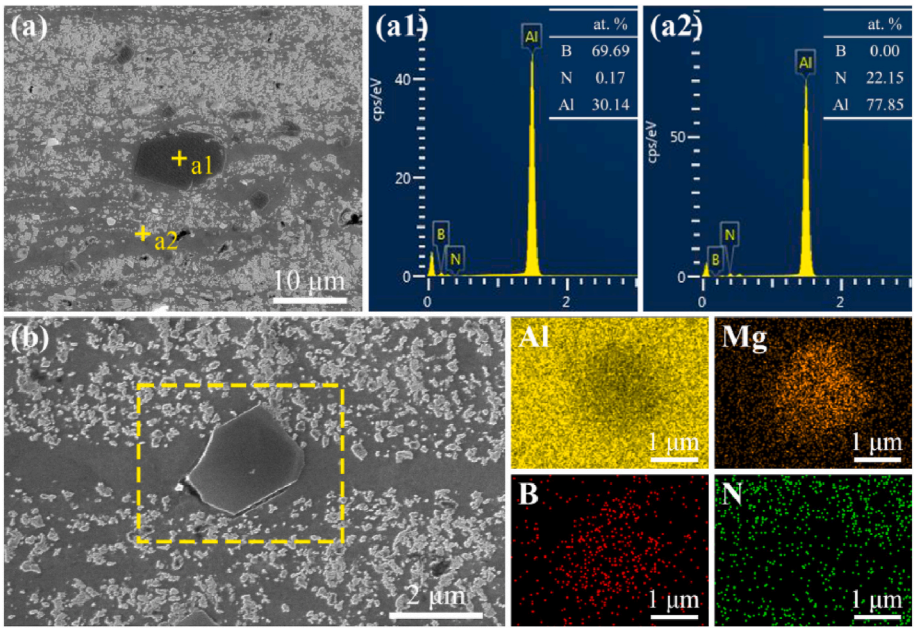

Fig. 4. The SEM morphologies and EDS analysis of (a-a2) AlN_p/Al; (b) AlN_p/Al–1Mg.

free zone became continuous banded along the extrusion direction and its width was decreased. Just a few narrow particle-free bands could be observed when the Mg content increased to 5% (Fig. 3d). Moreover, the amount of larger particles decreased significantly with increasing Mg content.

The microscopic distribution of AlN_p was further investigated by SEM at high magnification (Fig. 3a1–d1). Many large AlN_p agglomerated zones were observed in AlN_p/Al, as indicated by the yellow circle in Fig. 3a1. However, the agglomeration was significantly reduced with the addition of Mg. In addition, as indicated by the yellow arrow in Fig. 3c1, a few rectangular particles were observed in AlN_p/Al–3Mg and their number increased significantly when the Mg content up to 5%. The longitudinal direction of the rectangular particles was parallel to the extrusion direction with the length is about 0.5–1 μm and the aspect ratio is about 5.

In order to investigate the possible reasons for the change of the larger particles, EDS analysis was carried out for the micron sized particles in AlN_p/Al–1Mg (Fig. 4b), and an enrichment of Mg and B was evidently observed. It is known that B will form AlB_2 and MgB_2 with Al and Mg respectively, and both of these di-borides crystallize in hexagonal (P6/mmm) structure with alternating layers of metal atoms and B atoms [24], as shown in Fig. 5a. However, the $Al_xMg_{(1-x)}B_2$ compound has a lower formation enthalpy (ΔH_{form}) than the mixture of AlB_2 and MgB_2, as calculated by DFT (Fig. 5b and Table S1), and $AlMgB_4$ has the lowest ΔH_{form}. It is indicating that the compound is more stable than the mixture.

Therefore, as the percentage of Mg increases, the Al atomic positions in AlB_{2p} have a tendency to be gradually substituted by Mg atoms and eventually transformed into $AlMgB_4$. Furthermore, AlB_2 is a large particle while $AlMgB_4$ is the dispersed small particle with a specific morphology. Therefore, it is supposed that $Al_xMg_{(1-x)}B_2$ was formed directly during the sintering process, instead of forming AlB_2 first and then Mg atoms replacing the Al atom positions.

The rectangular particle in AlN_p/Al–3Mg was further characterized by TEM, and it shows that the particle has a hexagonal shape on the top view (Fig. 6a) and a rectangular shape in the side view (Fig. 6b). Therefore, the newly formed particles in AlN_p/Al–3Mg could be inferred to be hexagonal prism in shape, which is same to the morphology of $AlMgB_4$ [25]. Corresponding selected area electron diffraction (SAED) results showed that the [0001] zone axis in the cross section and the [100] zone axis in the longitudinal section were parallel to the incident electron beam, respectively. Combined with the ΔH_{form} calculated by DFT, the newly particle in AlNp/Al–3Mg could be preliminarily inferred as $AlMgB_4$.

The HRTEM (Fig. 6c) was used to further confirm the crystal structure of the rectangular particle, and the characterized zone is shown by the yellow square in Fig. 6b. The interface between the particle and the matrix was clear with no reaction products were observed, indicating

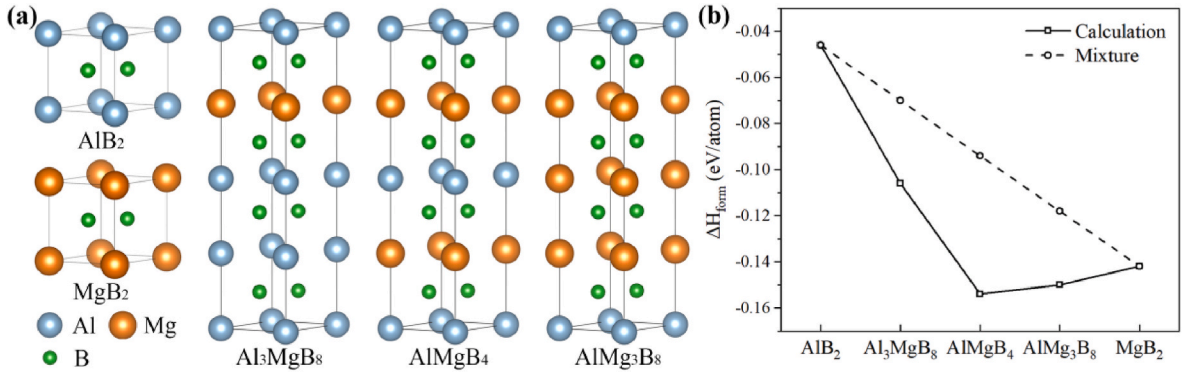

Fig. 5. (a) The crystal structure schematic diagram of $Al_xMg_{(1-x)}B_2$ (b) DFT calculated results of $Al_xMg_{(1-x)}B_2$.

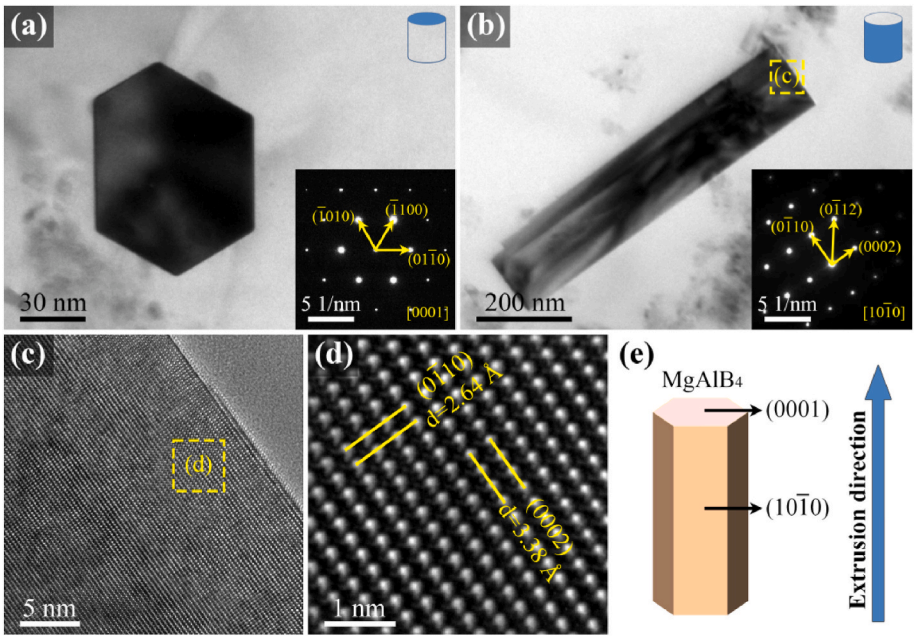

Fig. 6. The TEM images and corresponding SAED patterns of (a) the transverse section and (b) the longitudinal section of the rectangular particle; (c) the HRTEM image of the zone c in (b); the (d) 2D lattice phase images of zone d in (c); (e) Schematic microstructure diagram of $AlMgB_{4p}$.

that the particle and matrix were well bonded. The interplanar spacing of (0002) was about 3.38 Å and (0 $\bar{1}$ 10) was about 2.64 Å, measured from the 2D lattice phase (Fig. 6d). This structure showed a good consistency with the research of Serena Margadonna et al. [26] and PDF# 01-089-3178, so the rectangular particle was finally identified to be $AlMgB_4$ phase.

The distribution of AlN_p was further investigated by TEM. As shown in Fig. 7a, the grain of AlN_p/Al was elongated along the extrusion direction, while the AlN_p was distributed within the grain and at the grain boundary (as indicated by the yellow arrow). It was also clearly observed that the dislocation accumulated near the in-grain AlN_p (as indicated by the red arrow in the inset of Fig. 7a), and further formed the dislocation cell and sub-grain boundary, which indicated that the AlN_p can effectively pin dislocations and limit their slip in the grain.

The individual AlN_p were very small as observed at higher magnification (Fig. 7b), and the diameter is smaller than 50 nm. However, most AlN_p exists as multiple gathered particles and there is almost no Al between the gathered particles (as indicted by the red circle in Fig. 7b). Moreover, it was observed by HRTEM that the interface of AlN_p-Al was clean and no interfacial compounds. The FFT images and 2D lattice phase images for both sides of the interface are obtained from HRTEM image. The FFT images were consistent with diffraction patterns in the

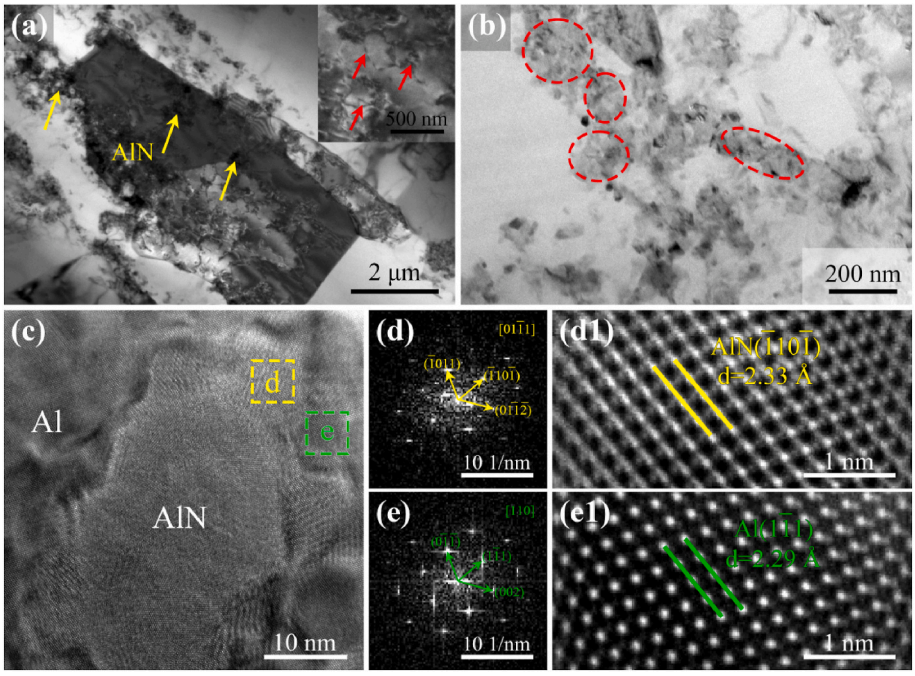

Fig. 7. The TEM images of (a) and (b) AlN_p/Al; the HRTEM image of (c) the AlN particle; the FFT and 2D lattice phase images of (d and d1) zone d and (e and e1) zone e in (c).

[01 $\bar{1}$ 1] zone axis of AlN_p and the [110] zone axis of Al, respectively, and the ($\bar{1}$ 10$\bar{1}$) crystal plane of AlN_p was parallel to the (1 $\bar{1}$ 1) crystal plane of Al. Therefore, the crystal orientation relationship between the AlN_p and Al matrix can be expressed as: $(\bar{1}\ 10\bar{1})_{AlN}//(1\ \bar{1}\ 1)_{Al}$, $[01\ \bar{1}\ 1]_{AlN}//[110]_{Al}$. The $(\bar{1}\ 10\bar{1})_{AlN}$ and $(1\ \bar{1}\ 1)_{Al}$ interplanar spacing were 2.33 Å and 2.29 Å, respectively.

3.2. Evolution of the matrix grains in AlN_p/Al-xMg

The morphology and distribution of the particle were significantly changed with different Mg contents, and Mg as an alloying element could be solid solution into the Al matrix. With the effect of these two factors, the morphology of the matrix grain may be altered. The grain morphology on the longitudinal section of AlN_p/Al-xMg was characterized by EBSD, as shown in Fig. 8. It is observed that the matrix was mainly elongated grains along the extrusion direction and the average grain diameter increased slightly after adding 1% Mg, and then decreased with the Mg content. The evolution of the grain morphology was also influenced by the particles, except for the fact that the Mg could lead to a grain refinement. Specifically, the strength of the particle-rich zone and particle-poor zone in AlN_p/Al was different, resulting in an inhomogeneous deformation during the extrusion process. The unstable plastic flow would make the particles cut through the matrix more often, which may lead to more cleavage of the grains and their refinement. Moreover, this unstable plastic flow was manifested by the curved interface between the particle-rich and particle-free bands in extruded samples, as shown in Fig. 3a. However, the deformation gradually became more uniform with the Mg content increased, which will be discussed in section 4.1, and the shearing effect of the particles on the matrix caused by the unstable plastic flow was also reduced. Subsequently, the particle distribution became more dispersed and could inhibit more dislocation movement than the agglomerated particles, which would have a contribution in grain refinement.

3.3. Mechanical properties of the AlN_p/Al-xMg composites

Fig. 9a shows the engineering stress-strain curves of AlN_p/Al-xMg tested at RT, and the details are given in Table 1. As the percentage of Mg increased, the yield strength (YS) and ultimate tensile strength (UTS) of the composite were significantly increased. Compared to AlN_p/Al, the UTS of the composites were increased by ~26.3%, ~66.9% and ~93.2% after adding 1%, 3% and 5% Mg, respectively. The ductility of the composites decreased relatively significantly after adding 1% Mg. However, there was only a slightly loss in ductility when Mg was further added, especially the strength of AlN_p/Al–5Mg was significantly higher than AlN_p/Al–3Mg, but the elongation (EL) was almost equal. Fig. 9c shows the comparison of the tensile properties for this work with other particle-reinforced aluminum matrix composites and Al–Mg alloys [19, 27–36]. As the Mg content increased, the properties of AlN_p/Al-xMg gradually broke through the "strength-toughness inversion" area, achieving an excellent synergistic strengthening of the reinforced particles and alloying elements.

To investigate the cryogenic properties of AlN_p/Al-xMg, uniaxial tensile tests were carried out at liquid nitrogen temperature (LNT), as shown in Fig. 9b. Compared with the RT tensile properties, all composites in this work showed a significant increase in strength at LNT, and these were accompanied by a decrease in elongation. However, the loss of ductility gradually decreased when more Mg was added as shown in Fig. 9d. In addition, the LNT tensile curve has almost no necking stage.

Tensile fracture surfaces are shown in Fig. 10. After fractured at RT, there are many small and shallow dimples (as indicated by the blue arrow) with some tearing edges on their top could be observed. The diameters of the dimples were decreased from about 2 μm to 0.5 μm after adding 5% Mg, indicating a decline in ductility and consistent with the tensile results. In addition, some large particles were observed at the bottom of the large dimples in AlN_p/Al and AlN_p/Al–1Mg (as indicated by the yellow arrow), which were AlB_{2p} and $Al_xMg_{1-x}B_{2p}$, respectively.

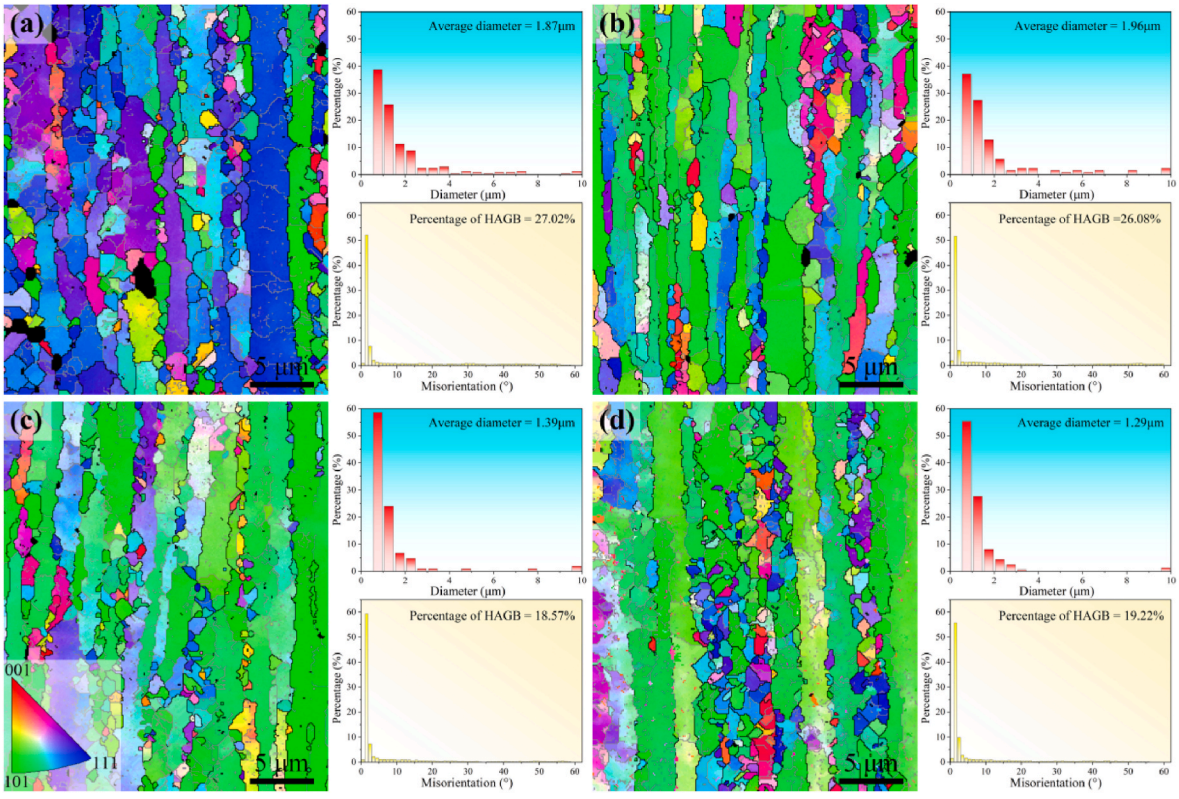

Fig. 8. The EBSD inverse pole figure maps and the corresponding distribution of grain size and orientation angles of adjacent grain boundaries in the longitudinal section of the (a) AlN_p/Al, (b) AlN_p/Al–1Mg, (c) AlN_p/Al–3Mg, (d) AlN_p/Al–5Mg.

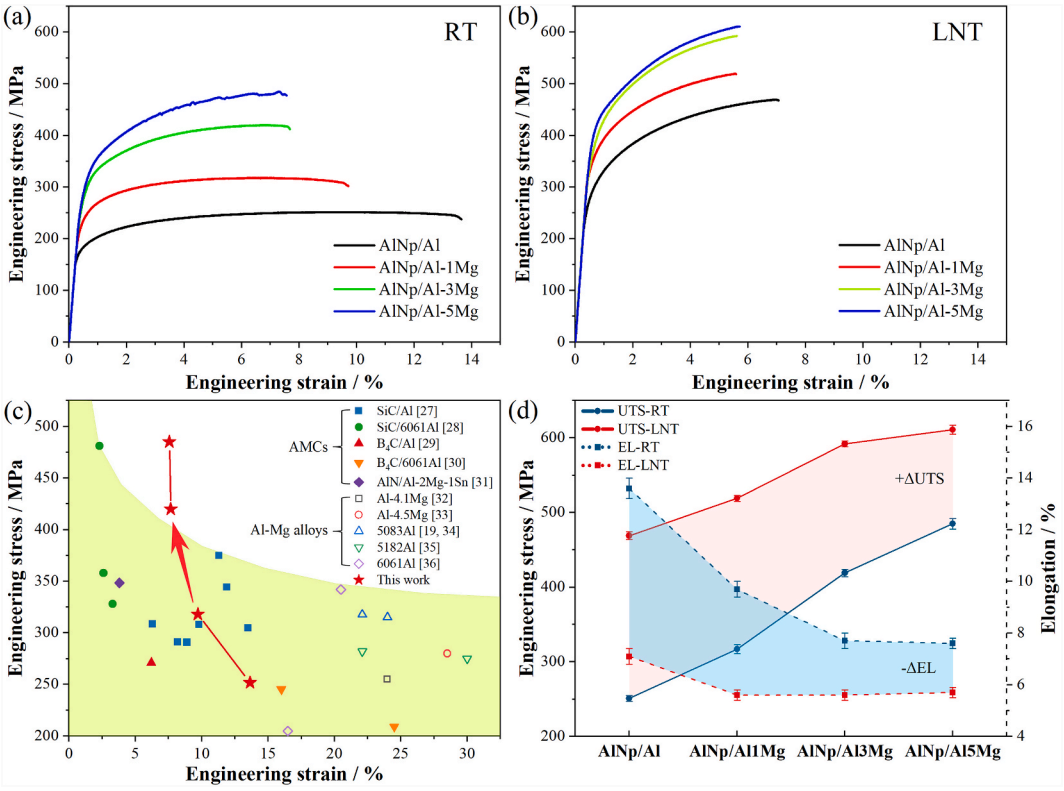

Fig. 9. Engineering stress-strain curves for AlN_p/Al-xMg tested at (a) RT and (b) LNT; (c) comparison of the tensile properties for this work with other particle-reinforced AMCs and Al–Mg alloys; (d) statistics of tensile properties for AlN_p/Al-xMg at RT and LNT.

Table 1
Tensile properties of AlN_p/Al-xMg at RT and LNT.

Samples	YS/MPa	UTS/MPa	EL/%
AlN_p/Al-RT	179 ± 2	251 ± 4	13.6 ± 0.4
AlN_p/Al–1Mg-RT	236 ± 2	317 ± 6	9.7 ± 0.3
AlN_p/Al–3Mg-RT	292 ± 1	419 ± 5	7.7 ± 0.3
AlN_p/Al–5Mg-RT	315 ± 5	485 ± 7	7.6 ± 0.2
AlN_p/Al-LNT	289 ± 3	469 ± 5	7.1 ± 0.3
AlN_p/Al–1Mg-LNT	359 ± 2	519 ± 4	5.6 ± 0.2
AlN_p/Al–3Mg-LNT	388 ± 4	592 ± 4	5.6 ± 0.2
AlN_p/Al–5Mg-LNT	420 ± 3	611 ± 6	5.7 ± 0.2

The surface of the particle was smooth, indicating that they were debonded from the matrix during the tensile process. In addition, part of the large particles cracked (as indicated by the yellow circle) which was due to the fact that they were large so the load could be transferred from the matrix to the particle during the tensile process, and eventually exceeded their strength limit.

After fractured at LNT, the proportion of the cracked particles was increased, which was because the matrix being strengthened at LNT, allowing a higher load could be transferred to the particle. In addition, traces of rapid tearing at the matrix and particle interface were observed, as shown in the inset of Fig. 10b1. This confirmed that once part of the particles had debonded from the matrix or cracked, the remaining areas could not resist the current load and caused a rapid fracture.

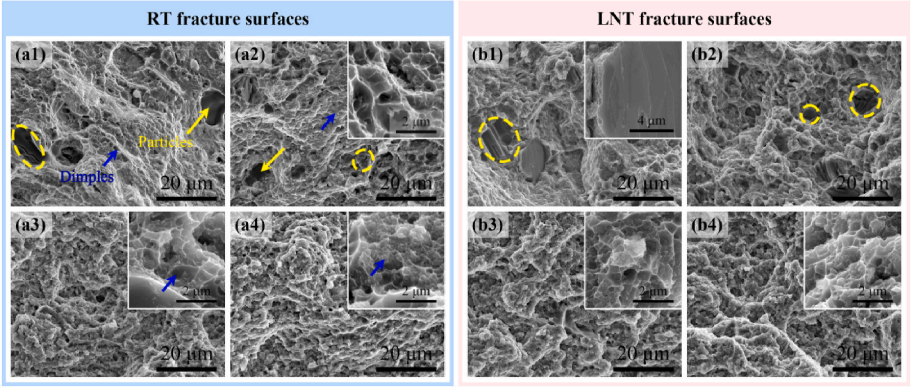

Fig. 10. The (a1-a4) RT and (b1-b4) LNT tensile fracture surfaces of (a1 and d1) AlN_p/Al, (a2 and b2) AlN_p/Al–1Mg, (a3 and b3) AlN_p/Al–3Mg, (a4 and b4) AlN_p/Al–5Mg.

4. Discussion

4.1. Evolution mechanism of particles

As reported in our previous work, there were AlN_p rich and lean domains in the sintered AlN_p/Al composites [37]. This is because the AlN_p was generated from nitrogen plasmid and Al by a solid-solid reaction, as shown in Fig. 11a–c. The nitrogen plasmid adheres uniformly to the surface of the Al powders after ball-milling. When the temperature reaches 580 °C, the nitrogen plasmid and Al react to form AlN_p, and release B atoms accordingly [38]. Moreover, due to the low solubility and the slow diffusion rate of N atoms in solid Al, the AlN_p forms mainly near the nitrogen plasmid powders. Then, as the temperature continues to rise, the AlN_p grow and cling to each other. Therefore, in the sintered composites, AlN_p is mainly distributed on the surface area of original Al powders, with the particle lean domain at the central area. Subsequently, during the extrusion process, the matrix exerts a shear stress on the AlN_p, causing the AlN_p to be distributed banded along the extrusion direction. Meanwhile, the flow of AlN_p can infill some particle lean domains, but cannot occupy the large particle-free domain. Therefore, if multiple pure Al powders were bonded together during the ball-milling process, no AlN_p can be formed internally, which ultimately results in the particle-free band after extrusion.

In contrast, as shown in Fig. 2d and e, the sharp edges of the Al–50Mg powder can hinder the polymerization of Al powders. This enables the BN plasmids to mix more uniformly with Al powders and react to form AlN_p, as shown in Fig. 11e and f, reducing the AlN_p lean domain, and subsequently resulted in a narrower particle-free band in the extruded sample. Meanwhile, with the addition of Al–50Mg powders, the sintered structure became more homogeneous, leading to the flow of the matrix became more stable during the extrusion process, which made the AlN_p band straighter.

In AlN_p/Al, the B atom released by nitrogen plasmids reacted with Al to form AlB_{2p} [38]. In AlN_p/Al-xMg (x≠0), the reaction product is $AlMgB_{4p}$ instead of AlB_{2p} and MgB_2 when Al, Mg and B co-exist at a certain temperature, which is because the $AlMgB_4$ has a more stable structure calculated by DFT. Therefore, it can be reasonably inferred that AlB_{2p} gradually transforms into $AlMgB_{4p}$ as the Mg content increases, and this is consistent with the experimental results. Regarding the fact that $AlMgB_{4p}$ is smaller than AlB_{2p}, the matrix can provide adequate Al atoms during the growth of the AlB_{2p} after nucleation. In contrast, the growth of $AlMgB_{4p}$ requires Mg atoms to diffuse to the nucleus, but atoms that are further away from the nucleation are unable to diffuse to the nucleation for the growth of $AlMgB_{4p}$. This allows a greater number, but smaller size of $AlMgB_{4p}$. In addition, in order to minimize the surface energy during growth, the growth rate of the $AlMgB_4$ nuclei in the [0001] orientation is faster than that in the [100] orientation [25]. Therefore, the generated $AlMgB_{4p}$ is hexagonal prism, and then the severe plastic deformation of the matrix during extrusion causes its long axis to be parallel to the extrusion direction.

4.2. Effect of particles and Mg element on the fracture mechanism

The size and distribution of particles were changed significantly with the addition of Mg, which would also make an important effect on the deformation of the matrix during the tensile process. As shown in Fig. 12, the side morphology of AlN_p/Al-xMg samples after tensile fracture was characterized by SEM. In AlN_p/Al, large surface reliefs were observed and the step pattern was divided into two types, at 45° to the tensile direction (as indicated by the yellow dotted line) and parallel to the fracture surface (as indicated by the blue dotted line), respectively. The step at 45° to the tensile direction was mainly concentrated at the boundary between the particle-rich zone and particle-free zone. This was due to the inhomogeneous distribution of particles resulted in an unequal distribution of stresses during the tensile process. The concentration of stresses caused the different local deformations and thus allowed for the surface relief. As the particle-free band narrowed and the boundary became straighter, the stress concentration was mitigated and then the steps gradually disappeared. The step parallel to the fracture surface was mainly found near to the fracture surface and there was also the necking area of the sample. The large deformation of the matrix and the reduction in the cross-section of the sample during the necking process resulted in the step parallel to the fracture surface.

In addition, by the side morphology of the fractured sample, it can be directly observed that the large particle debonded from the matrix or cracked after tensile deformation. Severe stress concentrations would be developed at the edges of the hole. As the deformation increased, the hole would expand which probably lead to the premature failure of the sample. These holes were also harmful to maintaining the ductility at cryogenic temperature, as an important reason that AlN_p/Al ductility decreased more at LNT.

4.3. RT strengthening mechanisms for AlN_p/Al-xMg composites

From the above research, it is known that the grain morphology and the size and distribution of the particle in AlN_p/Al-xMg were significantly altered by the addition of Mg. The strengthening mechanism of the AlN_p/Al-xMg is investigated in this section. This composites is

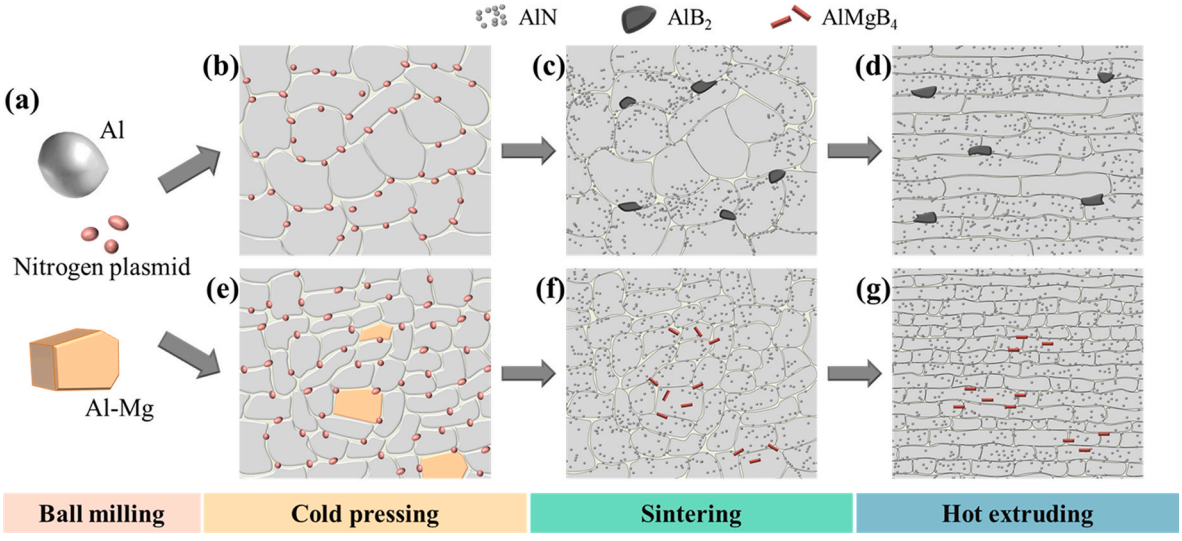

Fig. 11. Schematic representation of the particle generation process in (a–d) AlN_p/Al and (e–g) AlN_p/Al-xMg.

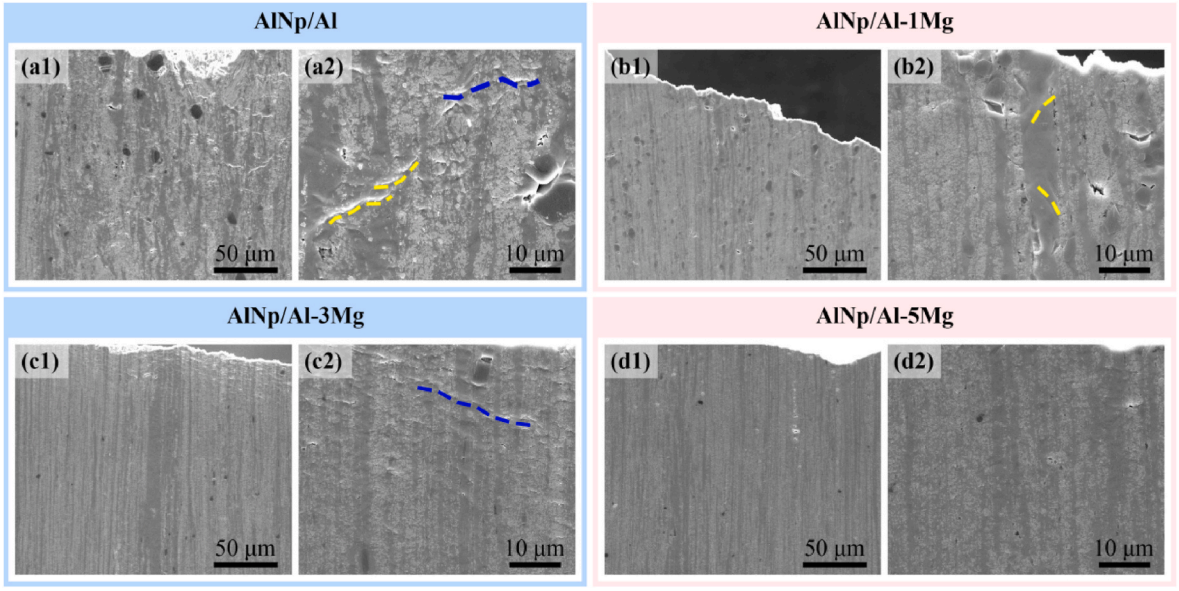

Fig. 12. The side morphology of (a1 and a2) AlN_p/Al, (b1 and b2) AlN_p/Al–1Mg, (c1 and c2) AlN_p/Al–3Mg and (d1 and d2) AlN_p/Al–5Mg samples after fracture at RT.

strengthened by both alloying elements and particles, so there are multiple strengthening mechanisms that can affect the yield strength (σ0.2), as indicated by follows [39]:

$$\sigma_{0.2} = \sigma_0 + \Delta\sigma_{ss} + \Delta\sigma_{GB} + \Delta\sigma_d + \Delta\sigma_{Orowan} + \Delta\sigma_{L-T} \quad (2)$$

where σ_0 (≈10 MPa) is the yield strength of Al single crystals [40]; $\Delta\sigma_{ss}$ is solid solution strengthening; $\Delta\sigma_{GB}$ is grain boundary strengthening; $\Delta\sigma_d$ is dislocation strengthening; $\Delta\sigma_{Orowan}$ is the Orowan strengthening and $\Delta\sigma_{L\text{-}T}$ is load transmitting strengthening.

The Portevin-Le Chatelier (PLC) in AlN_p/Al–5Mg stress-strain curve indicates that Mg not only reacts with Al and B to form $Al_xMg_{1-x}B_{2p}$, but also solid solution into Al matrix. The solid solution of Mg atoms cause lattice distortion and inhibit the dislocation movement, which can be expressed as follows [41]:

$$\Delta\sigma_{ss} = HC^n \quad (3)$$

where C is the concentration of solid solution Mg in Al, which was obtained by the averaging of various EDS point analyses in particle-free band (as shown in Figs. S2–S4 and Tables S2–S4); H and n are constants, $H = 13.8$MPa/(wt.% Mg) and $n = 1$ for Al–Mg alloys. In addition, the grain size of the matrix varied with the Mg content as shown in Fig. 8. Smaller grains mean more grains per unit volume and more grain boundaries to inhibit the dislocation movement during the deformation process. The contribution of grain boundaries to $\sigma_{0.2}$ can be described by the Hall-Petch formula [41]:

$$\Delta\sigma_{GB} = k_{H-P}d^{-1/2} \quad (4)$$

where k_{H-P} (=0.11 MPa/$m^{-1/2}$) is the Hall-Petch coefficient; d is the grain size of the composites. After extrusion, the dislocation in the matrix can impede the movement of new formed dislocations, resulting in dislocation piling, which increases the strength of the composites. Therefore, dislocation strengthening plays an important role in the strength of the composites. The relationship between strength and dislocation density can be expressed by the Bailey-Hirsch formula [42]:

$$\Delta\sigma_d = M\alpha Gb\rho_{GND}^{1/2} \quad (5)$$

where M (=3.06) is the Taylor factor of Al; α (≈0.24) is a constant; G (=25.4 GPa) is the shear modulus of Al; b (=0.286 nm) is the Burgers vector and ρ_{GND} is the geometrically necessary dislocations (GNDs) density. The density of GNDs can be calculated by the kernel average misorientation (KAM) that retrieved directly from the EBSD data (as shown in Fig. 13), and the exact formula is as follows [43]:

$$\rho_{GND} = \frac{2\theta_{KAM}}{xb} \quad (6)$$

Where x is unit length, which is equal to twice the step size used in EBSD acquisition and θ_{KAM} is the KAM. And KAM larger than 2° are excluded from the calculation, because it is assumed that they contribute to grain boundary strengthening.

Two particle strengthening mechanisms for composites are considered, which are the Orowan strengthening and load transmitting strengthening, respectively.

For AlN_p, its diameter is smaller than 50 nm (Fig. 7b), but in low magnification TEM images AlN_p was commonly observed in multiple tight clusters. Therefore, it could be inferred that the AlN phase observed in the SEM was multiple AlN_p tightly aggregated together, and the AlN_p approximate a spherical, so it was difficult to strengthen the matrix by load transfer during the tensile process. In addition, AlN_p is a ceramic particle that cannot be cut by dislocations and it can be inferred that the Orowan strengthening mechanism is the main one, expressed as follows [44]:

$$\Delta\sigma_{Orowan} = \frac{0.84MGb}{2\pi(1-\nu)^{1/2}\lambda}\ln\frac{2\bar{r}}{b} \quad (7)$$

$$\lambda = \bar{r} \bullet \left(\frac{2\pi}{3\varphi_{AlN}}\right)^{1/2} \quad (8)$$

where λ is the interspacing of particles; ν (=0.345) is the Poisson ratio of Al; $\bar{r}$ is the average effective radius and φ_{AlN} is the volume fraction of small particles (AlN_p), respectively. There is almost no Al between the tightly gathered AlN_p, so the average diameter counted by SEM is used as the effective diameter in calculation. In comparison, the AlB_{2p} has a larger volume and it was observed to crack in the fractured sample. $AlMgB_4$ has a high aspect ratio and the long axis is along the RD direction, i.e. the tensile direction. So it strengthens the composites mainly by sharing the load transferred from the matrix, and the strengthening effect can be expressed by the modified shear lag model:

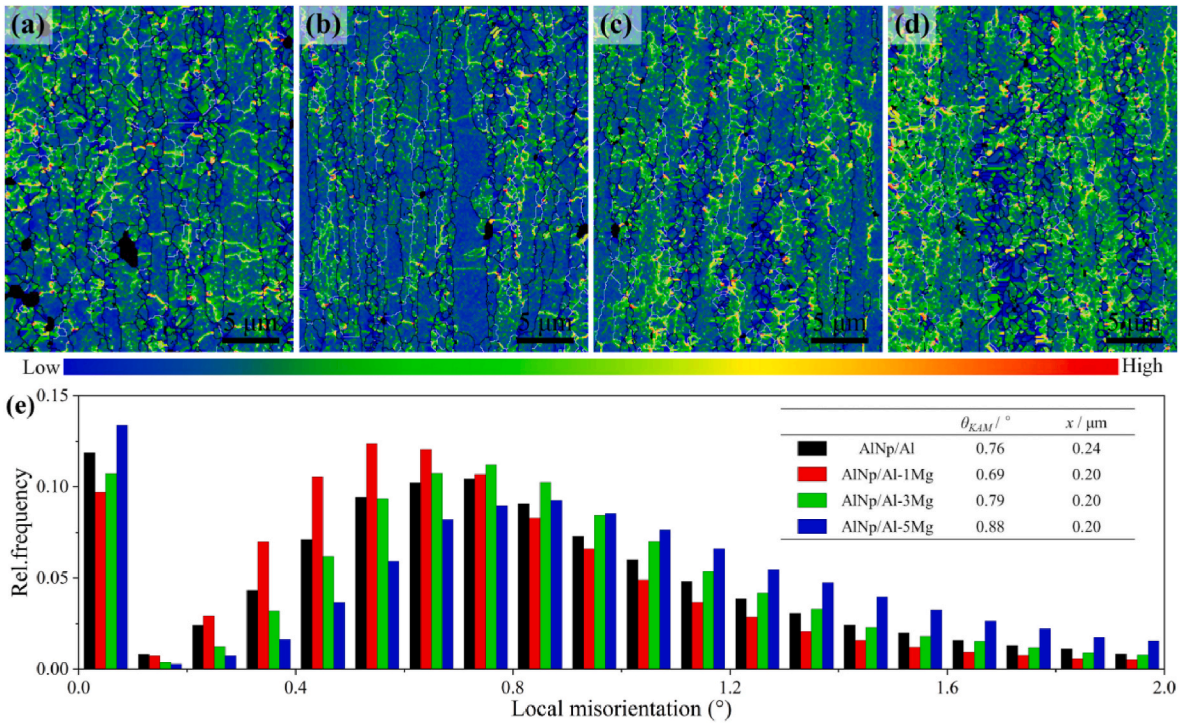

Fig. 13. The KAM map of the (a) AlN_p/Al, (b) AlN_p/Al–1Mg, (c) AlN_p/Al–3Mg and (d) AlN_p/Al–5Mg and corresponding (e) statistical histograms.

$$\Delta\sigma_{L-T} = \frac{1}{2}\sigma_{matrix}\left(\varphi_{AlB2}S_{AlB2} + \varphi_{AlMgB4}S_{AlMgB4}\right) \quad (9)$$

$$\sigma_{matrix} = \sigma_0 + \Delta\sigma_{SS} + \Delta\sigma_{GB} \quad (10)$$

Where σ_{matrix} is the YS of the matrix, φ_{AlB2} and φ_{AlMgB4} are the volume fraction of AlB_2 and $AlMgB_4$, S_{AlB2} (≈1) and S_{AlMgB4} (≈5) are corresponding effective aspect ratio.

As shown in Fig. 14, except for AlN_p/Al, the experimental and theoretical YS values of AlN_p/Al-xMg have a good match, and the detailed calculation process is shown in the Supplementary Materials. Deviations between experimental and theoretical YS values for AlN_p/Al probably resulted from the early debonding between AlB_{2p} and matrix, or the premature yielding of the wider particle-free band. In addition, of all strengthening mechanisms, $\Delta\sigma_{GB}$ and $\Delta\sigma_d$ make the largest contribution to YS, but the increase in yield strength of the composites with Mg content is mainly attributed to the increase of $\Delta\sigma_{SS}$ and the particle strengthening ($\Delta\sigma_{Orowan}$ and $\Delta\sigma_{L\text{-}T}$). This indicated that the addition of Mg to AlN_p/Al successfully further enhanced the composites and had a good theoretical basis, a synergistic strengthening by reinforcing particles and alloying elements was achieved.

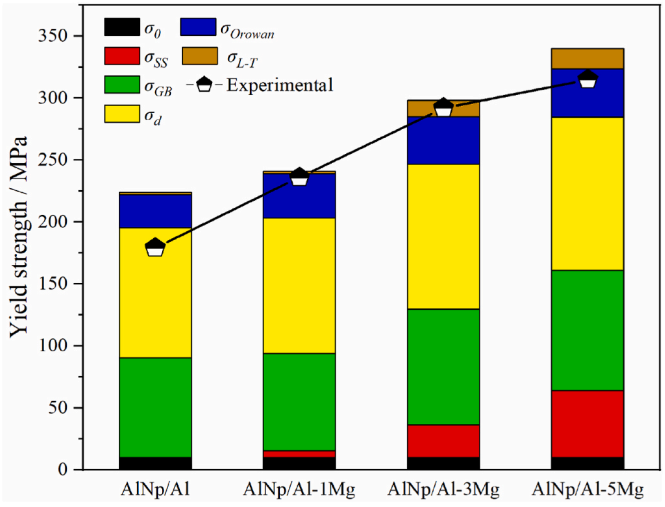

Fig. 14. Comparison between the experimental and theoretical yield strength of AlN_p/Al-xMg.

4.4. LNT strengthening mechanisms for AlN_p/Al-xMg composites

Fig. 15 illustrates the strain hardening rate (Θ) curves of the composites, which were derived from the true stress-strain curves (Fig. S5). As a function of true stress (σ_T) and true strain (ε_T), Θ represents the deformation resistance of the material to some extent.

The RT strain hardening rate curves show that the AlN_p/Al–5Mg has the highest Θ, and the slight wave on the AlN_p/Al–5Mg curve can attributed to the PLC instability of plastic flow. The dissolved Mg atoms, on the one hand, interact with the dislocations and inhibit their movement. On the other hand, it can reduce the SFE of the Al matrix [45], making the dislocation cross-slip become more difficult. This eventually leads to the increase of Θ. At LNT, the Θ was further increased compared with those at RT. When the temperature decreased to LNT, the Al matrix could store more dislocation and the dislocations become more difficult to slip, resulting in a higher density of defects during deformation (as shown in Fig. S6). Therefore, the strain hardening rate at LNT was increased, which contributed to the increase of UTS.

For the Al matrix, the yield strength ($\sigma_{y,m}$) can be divided into thermal contributions (σ_{th}) related to thermal activation of dislocation motion and temperature-independent non-thermal contributions (σ_{nth}), which expressed as follow [46]:

$$\sigma_{y,m} = \sigma_{th} + \sigma_{nth} \quad (11)$$

The σ_{th} can also be divided into two parts. One part is that the reduced atomic spacing leads to a stronger interatomic acting force, resulting in an increase in σ_0 and the grain boundary strength. The increased grain boundary strength contributes to the increased storage capacity of the dislocation. Another is that at cryogenic temperatures, the energy barrier for dislocation motion will be higher, so the enhanced

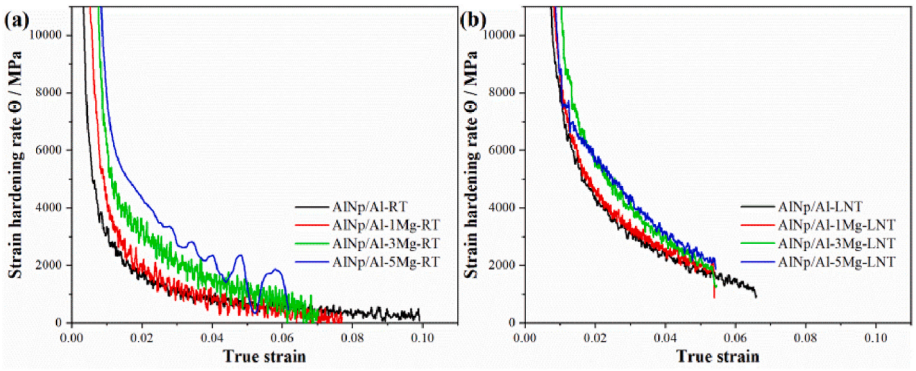

Fig. 15. The (a) RT and (b) LNT strain hardening rate curves for AlN_p/Al-xMg.

difficulty for dislocation slip will lead to an increase in strength.

For the reinforced particles, firstly, the difference in coefficient of thermal expansion (CTE) between the particles and the matrix will lead to an increase in dislocation density around the particles during cooling to LNT, which will increase the strength of the matrix and can be expressed as follow [47]:

$$\rho_{CTE} \approx \frac{6\Delta T \times \Delta CET \times \varphi_{particle}}{bd\left(1-\varphi_{particle}\right)} \tag{12}$$

$$\Delta\sigma_{CET} = M\beta Gb\rho_{CET}^{-1/2} \tag{13}$$

where the ρ_{CET} is the increased dislocation density during the cooling process; ΔT is the change of the temperature; ΔCET is the difference in CET between the matrix and the particles; d and $\varphi_{particle}$ is the mean diameter and the volume fraction of the particles, respectively; $\Delta\sigma_{CET}$ is the increase of strength caused by this mechanism; β is a constant.

Secondly, changes of shear modulus and Burgers vector have an effect on Orowan strengthening mechanism. The shear modulus will increase about 3.1–4.6 GPa when the temperature is lowered to 77K [48,49]. The CET of Al is about 2.4×10^{-5} K, so the change in lattice constant at LNT compared to RT will be less than 0.5%. Therefore, the change in the Burgers vector will not be taken into account and the increase in Orowan strengthening ($\Delta\sigma_{Orowan\text{-}LNT}$) as the temperature decreases to LNT can be expressed as follow:

$$\Delta\sigma_{Orowan-LNT} = \frac{G+\Delta G}{G}\Delta\sigma_{Orowan} \tag{14}$$

where the ΔG is the increase of shear modulus. In addition, the increased strength of the matrix also allows more load transfer from matrix to particle, corresponding to the increase in load transmitting strengthening. Therefore, the total increase of the strength from RT to LNT ($\Delta\sigma_{R\text{-}L}$) can be expressed as follows:

$$\Delta\sigma_{R-L} = \Delta\sigma_{th} + \Delta\sigma_{CET} + \Delta\sigma_{orowan-LNT} +$$

$$\frac{1}{2}\left(\Delta\sigma_{th} + \Delta\sigma_{CET}\right)\left(\varphi_{AlB2}S_{AlB2} + \varphi_{AlMgB4}S_{AlMgB4}\right) \tag{15}$$

where the $\Delta\sigma_{th}$ is the increase of σ_{th} from RT to LNT.

For the EL at LNT, when the applied stress reaches a specific stress, debonding may arise at the particle and matrix interface, forming holes and as the source of cracks. Meanwhile, the remaining areas could not resist the stress in this case, and the cracks expanded rapidly and coalesced with other cracks. This ultimately resulted in the immediate failure of the composites at maximum stress at LNT. Thus, the loss of ductility decreased with the increased Mg content, was probably related to the particle size became smaller and more uniform, which could reduce severe stress concentrations to some extent.

5. Conclusions

In summary, Mg elements introduced into AlN_p/Al resulted in a significant alteration of the microstructure and an improvement in the room and cryogenic temperature properties of the composites. The synergistic strengthening of reinforcing particles and alloying elements was achieved and the strengthening mechanism was analyzed in detail. The main conclusions are as follows:

(1) With the addition of Mg elements, small sized $AlMgB_{4p}$ formed instead of the large AlB_{2p}. The effective particle diameter of AlN_p decreased and its distribution in the matrix became more dispersed.
(2) The average grain diameter increased slightly and then decreased with Mg content, and the proportion of equiaxed crystals increased. This was not only related to the Mg content but also influenced by the unstable plastic flow during the extrusion process caused by the uneven particle distribution.
(3) The strength of AlN_p/Al-xMg increased significantly with Mg content at both room and cryogenic temperatures, and the loss of ductility at cryogenic temperatures gradually decreased, which was due to the more uniform microstructure avoiding crack generation.
(4) The lower formation enthalpy of $AlMgB_{4p}$ dominated the transformation of particle kinds, and the addition of AlMg powder allowed for a more uniform in-situ particle generation.
(5) Grain boundary strengthening and dislocation strengthening contributed mainly to the YS of the composites, but the increase in YS was mainly due to the increase of solid solution strengthening and particle strengthening. In addition, the combined strengthening mechanisms also contributed to the increase of the strength at LNT.

Credit authorship contribution statement

Xinda Sun: Investigation, Writing-original draft, Writing-review & editing. **Jinfeng Nie**: Conceptualization, Funding acquisition, Supervision, Writing – review & editing. **Yong Fan**: Data analysis. **Yuyao Chen**: Data analysis. **Xiangfa Liu**: Supervision. **Yonghao Zhao**: Supervision, Writing – review & editing.

Declaration of competing interest

The authors declare that they have no known competing financial interests or personal relationships that could have appeared to influence the work reported in this paper.

Data availability

Data will be made available on request.

Acknowledgements

The authors are grateful to the National Natural Science Foundation of China (Nos. 52271033 and 52071179), the Key program of National Natural Science Foundation of China (51931003), Natural Science Foundation of Jiangsu Province, China (No. BK20221493), Jiangsu Province Leading Edge Technology Basic Research Major Project (No. BK20222014), Foundation of "Qinglan Project" for Colleges and Universities in Jiangsu Province.

Appendix A. Supplementary data

Supplementary data to this article can be found online at https://doi.org/10.1016/j.compositesb.2023.111056.

References

[1] Dursun T, Soutis C. Recent developments in advanced aircraft aluminium alloys. Mater Des 2014;56:862–71.
[2] Xue H, Yang C, De Geuser F, Zhang P, Zhang JY, Chen B, Liu FZ, Peng Y, Bian JJ, Liu G, Deschamps A, Sun J. Highly stable coherent nanoprecipitates via diffusion-dominated solute uptake and interstitial ordering. Nat Mater 2022;22:434–41.
[3] Ma YH, Liu CL, Miao KS, Wu H, Li RG, Li XW, Fan GH. Effects of cooling rate and cryogenic temperature on the mechanical properties and deformation characteristics of an Al-Mg-Si-Fe-Cr alloy. J Alloys Compd 2023;947:169559.
[4] Nie JF, Chen YY, Chen X, Liu XF, Liu GL, Zhao YH, Zhu YT. Stiff, strong and ductile heterostructured aluminum composites reinforced with oriented nanoplatelets. Scripta Mater 2020;189:140–4.
[5] Theja PC, Suresh R, Reddy MCS. A review on - fabrication and testing methods of aluminium metal matrix nano composites for various applications. Mater Today Proc 2022;56:1137–42.
[6] Wu YM, Zhou C, Wu R, Sun LX, Lu CY, Xiao YZ, Su ZX, Gong MY, Ming KS, Liu K, Gu C, Yang WS, Wang J, Wu GH. Synergistic strengthening of Al–SiC composites by nano-spaced SiC-nanowires and the induced high-density stacking faults. Compos B Eng 2023;250:110458.
[7] Li PY, Li XN, Liu ZY, Chen LQ, Xiao BL, Ma ZY. Enhanced strength–ductility synergy of carbon nanotube/Al–Cu–Mg composites via introducing laminate structure and grain modification. Compos B Eng 2022;243:110178.
[8] Wang FC, Zhang JF, Sun KX, Quan LW, Wang J, Zhao NQ, Shi CS, Zheng SJ. Synergistic reinforcement effect of Fe and in-situ synthesized MgAlB4 whiskers in Al matrix composites. Compos B Eng 2022;246:110267.
[9] Gill RS, Samra PS, Kumar A. Effect of different types of reinforcement on tribological properties of aluminium metal matrix composites (MMCs) – a review of recent studies. Mater Today Proc 2022;56:3094–101.
[10] Law E, Pang SD, Quek ST. Effects of particle arrangement and particle damage on the mechanical response of metal matrix nanocomposites: a numerical analysis. Acta Mater 2012;60(1):8–21.
[11] Yang ZY, Fan JZ, Liu YQ, Yang ZY, Kang YL, Nie JH. Effect of combination variation of particle and matrix on the damage evolution and mechanical properties of particle reinforced metal matrix composites. Mater Sci Eng, A 2021;806:140804.
[12] Qian W, Zhao YT, Kai XZ, Yan YF, Tao R, Gao X. Synergistic reinforcement of in situ (ZrB2+TiB2) particles and Er on microstructure and properties of 6082Al matrix composites. J Alloys Compd 2020;813:152198.
[13] Gao X, Kai XZ, Du CC, Sun KL, Guan C, Zhu HF, Qian W, Zhao YT. Improved strength and ductility on laser beam welded joints of 7085Al matrix nanocomposites by in-situ ZrB2 nanoparticles and Al3(Er, Zr) nanoprecipitates. Compos B Eng 2023;266:110990.
[14] Ma X, Zhao YF, Zhao XJ, Nie JF, Chen HW, Liu XF. Mechanisms on the outstanding high temperature plasticity of AlNp/Al–0.4Cu composites induced by cryogenic treatment. J Alloys Compd 2019;770:755–64.
[15] Xie KW, Nie JF, Ma X, Liu XF. Increasing the ductility of heat-resistant AlNp/Al composites by submicron Al2O3 particles. Mater Char 2020;170:110672.
[16] Ren L, Gao T, Nie JF, Liu GL, Liu XF. A novel core-shell TiCx particle by modifying TiCx with B element and the preparation of the (TiCx + AlN)/Al composite. J Alloys Compd 2022;894:162448.
[17] Wang XS, Wang XZ, Liu K, Cao H, Su YS, Zhang D, Ouyang QB. Effect of the CNTs into SiCp-Al interfacial micro-zones on ageing precipitation behavior, microstructure and mechanical properties of SiCp(CNT)/Al–Zn–Mg–Cu composites. Compos B Eng 2023;259:110708.
[18] Zhu SZ, Wang D, Xiao BL, Ma ZY. Effects of natural aging on precipitation behavior and hardening ability of peak artificially aged SiCp/Al-Mg-Si composites. Compos B Eng 2022;236:109851.
[19] Son K, Kassner ME, Lee TK, Lee JW. Mg effect on the cryogenic temperature toughness of Al-Mg alloys. Mater Des 2022;224:111336.
[20] Guan L, Zhou Y, Zhang B, Wang JQ, Han EH, Ke W. Influence of aging treatment on the pitting behavior associated with the dissolution of active nanoscale β-phase precipitates for an Al–Mg alloy. Corrosion Sci 2016;103:255–67.
[21] Blöchl PE. Projector augmented-wave method. Phys Rev B 1994;50(24):17953–79.
[22] Perdew JP, Burke K, Ernzerhof M. Generalized gradient approximation made simple. Phys Rev Lett 1996;77(18):3865–8.
[23] Duan YH, Sun Y, Feng J, Peng MJ. Thermal stability and elastic properties of intermetallics Mg2Pb. Phys B Condens Matter 2010;405(2):701–4.
[24] Goswami R, Qadri SB. Suppression of Samson phase formation in Al-Mg alloys by boron addition. Mater Lett 2017;200:21–3.
[25] Wang FC, Li JJ, Shi CS, Liu EZ, He CN, Zhao NQ. In-situ synthesis of MgAlB4 whiskers as a promising reinforcement for aluminum matrix composites. Mater Sci Eng, A 2019;764:138229.
[26] Margadonna S, Prassides K, Arvanitidis I, Pissas M, Papavassiliou G, Fitch AN. Crystal structure of the Mg1-xAlxB2 superconductors near x≈0.5. Phys Rev B 2002;66(1):014518.
[27] Liu K, Su YS, Wang XZ, Cai YP, Cao H, Ouyang QB, Zhang D. Achieving simultaneous enhancement of strength and ductility in Al matrix composites by employing the synergetic strengthening effect of micro- and nano-SiCps. Compos B Eng 2023;248:110350.
[28] Xin L, Yang WS, Zhao QQ, Dong RH, Liang X, Xiu ZY, Hussain M, Wu GH. Effect of extrusion treatment on the microstructure and mechanical behavior of SiC nanowires reinforced Al matrix composites. Mater Sci Eng, A 2017;682:38–44.
[29] Guo H, Zhang ZW, Zhang Y, Cui Y, Sun LX, Chen D. Improving the mechanical properties of B4C/Al composites by solid-state interfacial reaction. J Alloys Compd 2020;829:154521.
[30] Gao MQ, Chen ZN, Li LW, Guo EY, Kang HJ, Xu YJ, Wang TM. Microstructure and enhanced mechanical properties of hybrid-sized B4C particle-reinforced 6061Al matrix composites. Mater Sci Eng, A 2021;802:140453.
[31] Balog M, Krizik P, Svec P, Orovcik L. Industrially fabricated in-situ Al-AlN metal matrix composites (part A): processing, thermal stability, and microstructure. J Alloys Compd 2021;883:160858.
[32] Liu Y, Liu MP, Chen XF, Cao Y, Roven HJ, Murashkin M, Valiev RZ, Zhou H. Effect of Mg on microstructure and mechanical properties of Al-Mg alloys produced by high pressure torsion. Scripta Mater 2019;159:137–41.
[33] Li ZZ, Li XY, Yan HG, Chen JH, Xia WJ, Li Q, Su B, Song M. Achieving high damping and excellent ductility of AlMg alloy sheet by the coupling effect of Mg content and fine grain structure. Mater Char 2021;174:110974.
[34] Ma MY, Lai RL, Qin J, Wang B, Liu HQ, Yi DQ, Zhai TG. Achieving exceptionally tensile properties and damage tolerance of 5083 aluminum alloy by friction stir processing assisted by ultrasonic and liquid nitrogen field. Mater Sci Eng, A 2021;806:140824.
[35] Meng XC, Liu B, Luo L, Ding Y, Rao XX, Hu B, Liu Y, Lu J. The Portevin-Le Châtelier effect of gradient nanostructured 5182 aluminum alloy by surface mechanical attrition treatment. J Mater Sci Technol 2018;34(12):2307–15.
[36] Knowles AJ, Jiang X, Galano M, Audebert F. Microstructure and mechanical properties of 6061 Al alloy based composites with SiC nanoparticles. J Alloys Compd 2014;615:S401–5.
[37] Lu FH, Nie JF, Ma X, Li YS, Jiang ZW, Zhang Y, Zhao YH, Liu XF. Simultaneously improving the tensile strength and ductility of the AlNp/Al composites by the particle's hierarchical structure with bimodal distribution and nano-network. Mater Sci Eng, A 2020;770:138519.
[38] Ma X, Zhao YF, Tian WJ, Qian Z, Chen HW, Wu YY, Liu XF. A novel Al matrix composite reinforced by nano-AlNp network. Sci Rep 2016;6(1):34919.
[39] Ma LS, Zhang X, Duan YH, Zhang HW, Ma N, Zhu L, Rong XD, Zhao DD, He CN, Zhao NQ. Achieving exceptional high-temperature resistant Al matrix composites via two-dimensional BN pinning grain rotation. Compos B Eng 2023;253:110570.
[40] Jobba M, Mishra RK, Niewczas M. Flow stress and work-hardening behaviour of Al–Mg binary alloys. Int J Plast 2015;65:43–60.
[41] Malopheyev S, Kulitskiy V, Kaibyshev R. Deformation structures and strengthening mechanisms in an AlMgScZr alloy. J Alloys Compd 2017;698:957–66.
[42] Ma KK, Wen HM, Hu T, Topping TD, Isheim D, Seidman DN, Lavernia EJ, Schoenung JM. Mechanical behavior and strengthening mechanisms in ultrafine grain precipitation-strengthened aluminum alloy. Acta Mater 2014;62:141–55.
[43] Liu YF, Cao Y, Mao QZ, Zhou H, Zhao YH, Jiang W, Liu Y, Wang JT, You ZS, Zhu YT. Critical microstructures and defects in heterostructured materials and their effects on mechanical properties. Acta Mater 2020;189:129–44.
[44] Li YJ, Muggerud AMF, Olsen A, Furu T. Precipitation of partially coherent α-Al(Mn, Fe)Si dispersoids and their strengthening effect in AA 3003 alloy. Acta Mater 2012;60(3):1004–14.
[45] Zhao DD, Løvvik OM, Marthinsen K, Li YJ. Impurity effect of Mg on the generalized planar fault energy of Al. J Mater Sci 2016;51(14):6552–68.
[46] Gao M, Kang H, Chen Z, Guo E, Fu Y, Xu Y, Wang T. Enhanced strength-ductility synergy in a boron carbide reinforced aluminum matrix composite at 77 K. J Alloys Compd 2020;818:153310.
[47] Zheng R, Chen J, Zhang Y, Ameyama K, Ma C. Fabrication and characterization of hybrid structured Al alloy matrix composites reinforced by high volume fraction of B4C particles. Mater Sci Eng, A 2014;601:20–8.
[48] Voitenko AF, Skripnik YD, Solov'eva NG. Anisotropy of elasticity characteristics for a series of structural metals in the temperature from 4. 2 to 300°K. Strength Mater 1987;19(1):89–92.
[49] Naimon ER, Ledbetter HM, Weston WF. Low-temperature elastic properties of four wrought and annealed aluminium alloys. J Mater Sci 1975;10(8):1309–16.